Design of tungsten fiber-reinforced tungsten composites with porous matrix

Yiran Mao[a,b,*], Jan Coenen[b,f], Sree Sistla[c], Chao Liu[c], Alexis Terra[b], Xiaoyue Tan[a,b,d], Johann Riesch[e], Till Hoeschen[e], Yucheng Wu[a,d,f], Christoph Broeckmann[c], Christian Linsmeier[b]

[a] *School of Mechanical Engineering, Hefei University of Technology, Hefei 230009, China*

[b] *Forschungszentrum Jülich GmbH, Institut für Energie- und Klimaforschung - Plasmaphysik, Partner in the Trilateral Euregio Cluster, 52425 Jülich, Germany*

[c] *Institut für Werkstoffanwendungen im Maschinenbau (IWM), RWTH Aachen University, 52062 Aachen, Germany*

[d] *School of Material Science and Engineering, Hefei University of Technology, Hefei 230009, China*

[e] *Max-Planck-Institut für Plasmaphysik, 85748 Garching b. München, Germany*

[f] *Key Laboratory of Interface Science and Engineering of New Materials, Ministry of Education, Taiyuan University of Technology, Taiyuan 030024, China*

[g] *Department of Engineering Physics, University of Wisconsin Madison, WI 53706 Madison, USA*

*Corresponding author: Yiran Mao (y.mao@fz-juelich.de)

Abstract: To overcome the brittleness of tungsten, tungsten fiber-reinforced tungsten composites (W_f/W) have been developed using an extrinsic toughening mechanism. In this work, a novel type of W_f/W with porous matrix produced by field assisted sintering technology (FAST) is studied. The material is optimized regarding mechanical behavior, standing on the adjusting of matrix porosity and fiber mass fraction. Two series of samples with different matrix density and fiber mass fraction are prepared. Based on the mechanical testing, porous matrix

W_f/W can represent a promising pseudo ductile behavior. Relatively lower matrix density is helpful to avoid a sudden load-drop during crack opening. The different fracture behavior is attributed to the different fiber/matrix interface bonding condition. By increasing fiber mass fraction from 20% to 50%, porous matrix W_f/W can facilitate improved mechanical properties regarding fracture toughness and strength. However, by further increasing the fiber mass fraction from 50% to 60%, a deterioration of mechanical properties is observed. The high porosity of porous matrix W_f/W causes a degradation of the thermal conductivity compared to conventional bulk tungsten. No significant change regarding thermal expansion coefficient is observed when decreasing the matrix density.

Keywords: Fiber-reinforced composites, Porous matrix, Tungsten, Mechanical properties, Field assisted sintering technology

1. Introduction

Future energy systems, which range from concentrated solar power to fusion energy, rely on the development of materials for application under high thermal and thermal-cyclic loads. Due to its high melting point, high thermal conductivity and high temperature strength, tungsten is especially attractive when looking for high thermal exhaust and high operational temperature applications, like plasma facing materials in fusion reactor, receivers for concentrated solar power or refractory materials [1-3]. However, the intrinsic brittleness of tungsten is of great concern during operation with high transient heat loads [4]. To overcome the brittleness, many methods have been investigated to increase the toughness of W material, such as adding second phase particles, alloying or grain refinement [5-10]. However, the traditional intrinsic toughening methods, i.e. dispersion strengthening or grain refinement, have their limitations in

long-term high temperature application, especially in fusion environment. Under the effect of high temperature recrystallization during operation and neutron irradiation in fusion application which causes severe internal damages, the intrinsic toughening mechanism will gradually fail [11-13]. To overcome this issue, tungsten fiber-reinforced tungsten composites (W_f/W) are being developed relying on extrinsic toughening mechanisms [14-18]. With the incorporation of fibers, energy dissipating mechanisms, like ductile deformation of fibers, fiber pull-out, and crack bridging and deflection at the interface are facilitated, leading to extra energy consumption. The extrinsic toughening effect does not only rely on the intrinsic properties of the materials, rather on the interaction between the fibers and matrix. As long as the interface exists, the reinforcement will work to a certain extent. In recent studies, a process has been established to produce W_f/W using field assisted sintering technology (FAST) [14]. FAST is a low-voltage, pulsed direct current-activated, pressure-assisted sintering and synthesis technique. During this process, the fiber–powder mixture is consolidated to a bulk material by Joule heating under uniaxial pressure in a mold [19, 20]. With the help of a weak oxide interface or a porous matrix, a pseudo-ductile fracture behavior can be achieved, as demonstrated in previous studies [14]. Even with brittle fibers and matrix (in case after neutron irradiation or high temperature recrystallization in fusion environment), this material shows still improved tolerance towards cracking and damage compared to conventional tungsten, which makes this material an ideal plasma-facing material for future fusion reactors [21-23].

Porous matrix W_f/W contains low density tungsten matrix, using a controlled amount of fine-scale matrix porosity to realize the weak connection between fiber and matrix [23]. This approach can be viewed as an extension of the weak coating concept [24]. Damage tolerance

is obtained when the matrix acts as a mechanical 'buffer' between adjacent fibers so that the cracks from the matrix do not penetrate into the fibers. For this case, crack deflection occurs because of the low strength of the porous interphase and its poor cohesion with the fibers. Fiber breakage should remain isolated with minimal stress concentration in neighboring fibers. Porous matrix composites offer a possible alternative to conventional weak interface composites, which have a great advantage for largescale production due to the shunning of the costly fiber coating processes. This principle has also been widely used, for example in carbon fiber-reinforced carbon (CFC) or silicon carbide fiber-reinforced silicon carbide (SiC/SiC) [25]. However, the application of the fiber-reinforcement on porous metallic based materials is still novel.

In a recent work, this new concept was first time proposed and has been proven that, the porous matrix W_f/W can represent a promising pseudo ductile behavior [26]. Similar to other fiber reinforced ceramic composites, theoretically, fiber/matrix interface properties and fiber volume fraction of porous matrix W_f/W are the most important parameters which influence the mechanical properties of the composites. However, in previous studies, the discussion on this issue is still blank. The optimized fiber volume fraction and interface condition are still not explicit. Additionally, for damage tolerance, cracks in the matrix must be deflected into the fiber/matrix interface. The conditions for deflection of W_f/W are determined by the elastic mismatch (α) between fiber and matrix:

$$\alpha = (E_f' - E_m')/(E_f' + E_m') \quad (1)$$

Where E' is the plain strain modulus, 'm' and 'f' represent matrix and fiber respectively. The elastic mismatch (α) increases with the increasing matrix porosity, which is beneficial for crack

deflection. However, if the porosity is too high, the matrix will be too loose with very low material strength. Therefore, for a given fiber strength and mass fraction, there must be a sweat point of porosity to realize both increased damage tolerance without losing much of the material strength.

In this study, to optimize the porous matrix W_f/W, the influence of sample density and fiber mass fraction is studied. Series of samples with different density and fiber mass fractions are produced. Sample densities are varied by changing the sintering temperature during FAST process, as it is directly related to matrix density itself. Mechanical tests, including in-situ 3-point bending tests, 4-point bending test are performed to calculate the fracture toughness and flexural strength of the material. Thermal conductivity and coefficient of thermal expansion are also measured to prove effect of porosity and the fiber implantation.

2. Experimental

Manufacturing

Field assisted sintering technology (FAST) is used for the manufacturing of porous matrix W_f/W. Raw materials are pure tungsten powders (OSRAM GmbH) with 5 µm average particle size (fischer sub sieve size) and potassium doped short tungsten fibers (OSRAM GmbH) with 2.4 mm length and 0.15 mm diameter. The as-fabricated fiber is shown in Figure 1. The fibers are produced by a drawing process, therefore, a very fine and elongated grain structure is formed. Due to this grain structure, the tungsten fibers show good ductility (up to ~3% deformation) and extremely high tensile strength (up to 3000 MPa) [27, 28]. In order to increase the fiber microstructural stability, the fibers are doped with potassium (~75 ppm) during the fiber manufacturing. The potassium is insoluble in tungsten, forming nano-disperse rows of

bubbles along the elongated grains, which can pin the grain boundaries during the recrystallization process [29].

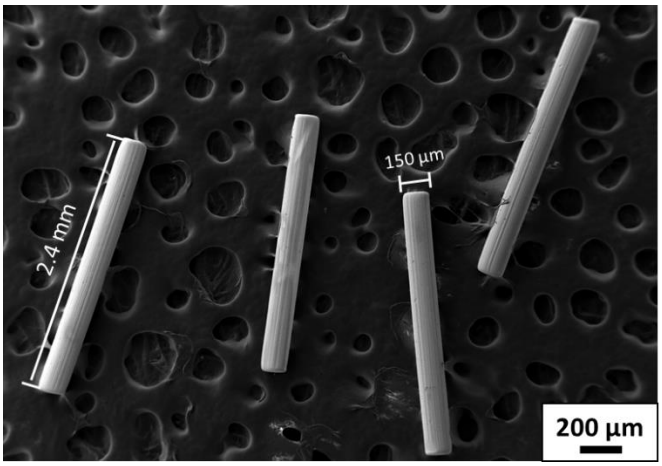

Figure 1 short tungsten fibers used for Wf/W production

For the consolidation process, the tungsten fibers and the powders are mixed by manual shaking in a vessel with various fiber mass fractions from 20%-60%. The mixture is then spread into a graphite mold with 40 mm diameter. Tungsten foils with a thickness of 0.025 mm are used between the to be sintered sample and the graphite mold to reduce the carbon contamination during sintering process [30, 31]. The sintering is performed in vacuum with a pressure below 0.1 mbar. As result, coin shape samples (40 mm diameter and ~5 mm height) are produced. Sample list with the corresponding sintering parameters is shown in Table 1. In total, 8 samples are prepared with two sintering temperature and different fiber mass fraction.

In previous study on pure W consolidated by SPS, the sintering temperature are normally in the range of 1900-2100°C to achieve a relative density above 95% [32, 33]. To find out the optimized porosity, a series of preliminary sintering temperature scan from 1300 °C to 1900 °C (1300 °C, 1400 °C, 1550 °C and 1900 °C) has been done. For the samples that sintered at 1300 °C and 1900 °C, the material properties are not ideal, which will be further discussed in Section 4. Therefore, this work will focus on the sample sintered at 1400 °C and 1550 °C.

The sintering time is based on the preliminary SPS experiments on W_f/W, showing that the punch displacement tends to be stable after 4 min at the holding temperature. In order to minimize the recrystallization of the W fibers, the sintering holding time is set to 4 min. The sintering pressure (60MPa) is determined by the maximum strength of the graphite tools used in this study.

The compaction method in SPS process has an influence on the fiber orientation, the fibers tends to oriented in the plane that is perpendicular to the pressing direction. In this study, all the microstructure analyses are performed on the surface that parallel to the compaction direction. For the bending tests, the sample loading direction is parallel to the compaction direction of SPS process.

Table 1 sintering parameters of W_f/W

Sintering parameters	**W_f/W1400**	**W_f/W1550**
Temperature	1400 °C	1550 °C
Pressure	60 MPa	60 MPa
Holding time	4 min	4 min
Heating rate	100 °C/min	100 °C/min
Fiber mass fraction	30%, 40%, 50%, 60%	20%, 40%, 50%, 60%

Characterization

After sintering, the sample mass density is measured by the Archimedes principle, followed by a series of mechanical and physical tests.

To study the fracture behavior, an in-situ 3-point bending test is performed. 3-point bending samples are manufactured based on the EU standards DIN EN ISO 148-1 and 14556: 2006–10

[34]. According to this standard the small size specimens have the following dimensions (KLST geometry) [35]: 3 mm x 4mm x 27 mm, 22 mm span, 1 mm V-notch depth, 0.1 mm notch root radius. All samples are cut by electrical discharge machining (EDM) without further surface and notch treatment.

The bending test is performed using a universal testing device (TIRAtest 2820, Nr. R050/01, TIRA GmbH). During the bending test (1 μm/s testing speed), an optical camera system (DU657M Toshiba) is used to track crack behavior and absolute sample movement. The sample displacement in this test is defined as the vertical movement of the sample relative to the reference stage. At the same time the corresponding force is also recorded. By this, a quantitatively measured force-displacement curve can be then determined. For each type of sample, 2 to 5 tests are performed.

Apart from the force-displacement curve, fracture toughness (K_q) can also be calculated based on ASTM E399 standard [36]. The calculation combines the stable crack growth length and the corresponding load during the test:

$$K_q = \frac{P \cdot S}{B \cdot W^{3/2}} \cdot f(a_f/W) \tag{2}$$

Where P is the maximum load during stable crack growing, S is the distance between the support pins, B is the sample width, W is the sample thickness, a_f is the stable crack length which equals to the pre-notch length plus the crack extension length, the geometric factor $f(a_f/W)$ is described in ASTM E399:

$$f\left(\frac{a_f}{W}\right) = \frac{3\left(\frac{a_f}{W}\right)^{\frac{1}{2}}\left\{1.99-\left(\frac{a_f}{W}\right)\left(1-\frac{a_f}{W}\right)\left(2.15-\frac{3.93a_f}{W}+\frac{2.7{a_f}^2}{W^2}\right)\right\}}{2\left(1+\frac{2a_f}{W}\right)\left(1-\frac{a_f}{W}\right)^{\frac{3}{2}}} \tag{3}$$

Here, the maximum stable crack extension length is measured as the surface crack length based

on the in-situ tracking image. The corresponding force before the unstable load drop is used as the maximum loading. Based on the force-displacement curves, the fracture energy is calculated by integrating the area below the curves, showing the energy consumption during fracture. In this calculation, when the force drops below 50N, the test is considered to be finished.

4-point bending tests are performed to measure the flexural strength. The 4-point bending test sample dimension is 20 × 2 × 2.25 mm^3 (length×width×thickness). The tests are applied by using an Instron 3342 universal testing machine (Instron GmbH). During the tests, the sample is set on two support pins with a distance of 18 mm. A pressing load from 2 load pins with a distance of 9 mm is applied in the middle of the sample. The load pins move with a constant speed (0.3 mm/min) during the test.

The maximum force of the test is record as the fracture force. The flexural strength can be calculated based on [37]:

$$\sigma_{flexural} = \frac{3F_b L_b}{4b_b h_b^2} \tag{4}$$

in which $\sigma_{flexural}$ is the flexural strength of the sample; F_b is the maximum force; L_b is the distance between the two support pins; b_b is the width of the sample and h_b is the height of the sample.

Thermal conductivity is measured from room temperature to 900 °C using a laser flash system (LFA457, MicroFlash). Here, disc shaped specimens with a diameter of 6 mm and thickness of 2 mm are used. The testing atmosphere is Ar. One sample produced at 1400 °C (W_f/W1400) with 40% fiber mass fraction is tested.

The microstructure of the sample cross section and the fracture surface are characterized by

scanning electron microscope (SEM, Zeiss Crossbeam 540, 30KV Maximum accelerating voltage), equipped with focused ion beam (FIB). To determine the mechanical properties of the fiber after sintering, hardness tests (HV1, Instron GmbH) are performed. The test force of the micro-hardness testing is 9.8N, the dwell time is 10 s to 15 s. For each data point, 10 indents are performed.

In a future energy system, tungsten, as amour materials, will be joint with the cooling structures. Therefore, the coefficient of thermal expansion (CTE) value is an important property for the component design. To determine the CTE, porous matrix W_f/W are tested by using a dilatometer with a temperature range between room temperature and 400 °C with a heating rate of 5 °C/min. Rod-shaped specimens with a diameter of 6 mm and a length of 20 mm are used for the measurement. The testing atmosphere is Ar, the tested sample is produced at 1550 °C (W_f/W1550) with 40% fiber mass fraction.

3. Results

The densities of different porous matrix W_f/W measured by Archimedes principle are shown in Table 2. As it can be seen from the results, the relative density of porous matrix W_fW increases with increasing fiber mass fraction when the fiber mass fraction is below 50%. This is because of the increasing content of the already dense fibers [38]. However, when the fiber mass fraction increases to 60%, the relative density decreases again. This effect can be attributed to the large voids formation sintering during the FAST process, which will be discussed in detail in the following part.

Table 2 sample density with different fiber mass fraction

	20%	30%	40%	50%	60%
W_f/W1400	-	75.4%±0.4%	77.3%±0.9%	80.0%±0.9%	79.6%±0.7%
W_f/W1550	80.3%±0.4%	-	85.1%±0.7%	87.0%±0.2%	81.0%±0.8%

The overview microstructure of the typical porous matrix W_f/W (40% fiber mass fraction) for both sintering temperature is shown in Figure 2. The microstructure of the fiber/matrix interface area are given in Figure 3. It can be seen that the porosity of the W_f/W1400 is higher than that of W_f/W1550 due to the lower sintering temperature. This affects the fiber/matrix bonding conditions. It can be observed from Figure 3 that a looser bonding between fiber and matrix is formed for W_f/W1400 compared to W_f/W1550.

Figure 4 shows the microstructure of sample Wf/W1440 with 60% fiber mass fraction, in which large voids/gaps can be seen. When the fiber mass fraction is too high, on one hand, there will be not enough powders to fill up the gaps between the fibers, on the other hand, powders cannot reach all the gaps between the fibers. In this case, the fibers will be in direct contact during the consolidation process without powders binding them, leaving voids after sintering.

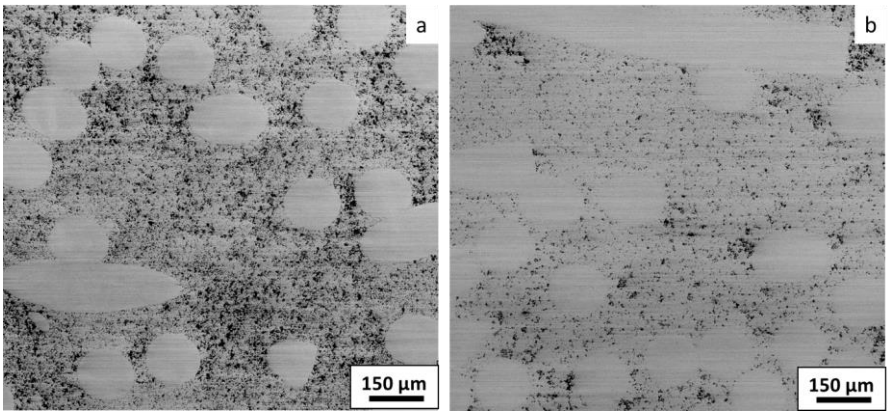

Figure 2 SEM image (SE, 10 kV accelerating voltage) of a): W_f/W1400 (1400 °C) and b): W_f/W1550 (1550 °C) with 40% fiber mass fraction showing the microstructure overview

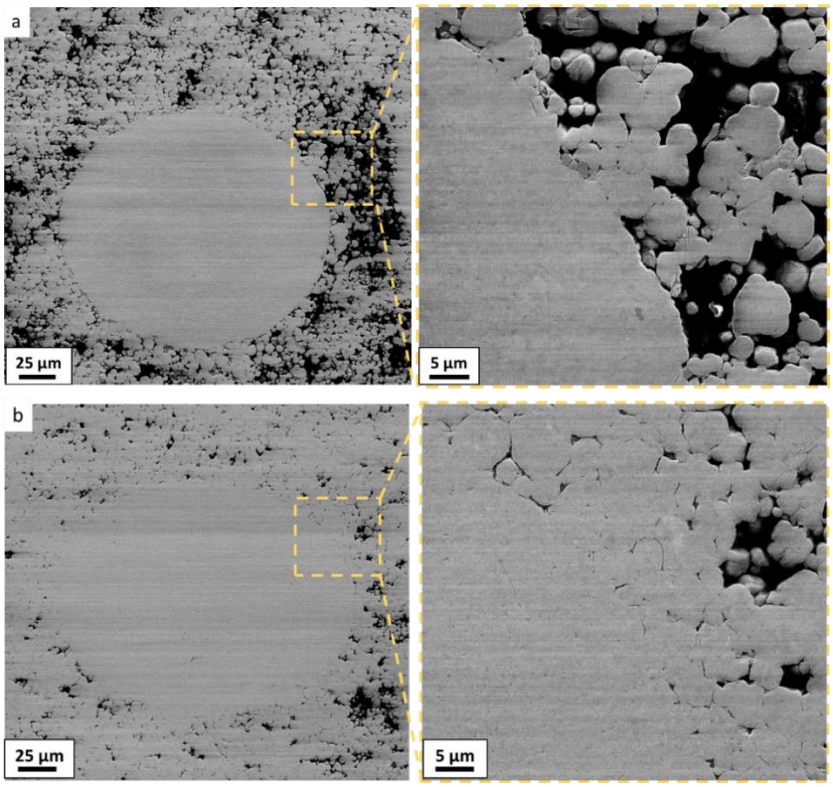

Figure 3 SEM image (SE, 10 kV accelerating voltage, SE) of a): W_f/W1400 (1400 °C) and b): W_f/W1550 (1550 °C) with 40% fiber mass fraction showing the fiber/matrix area

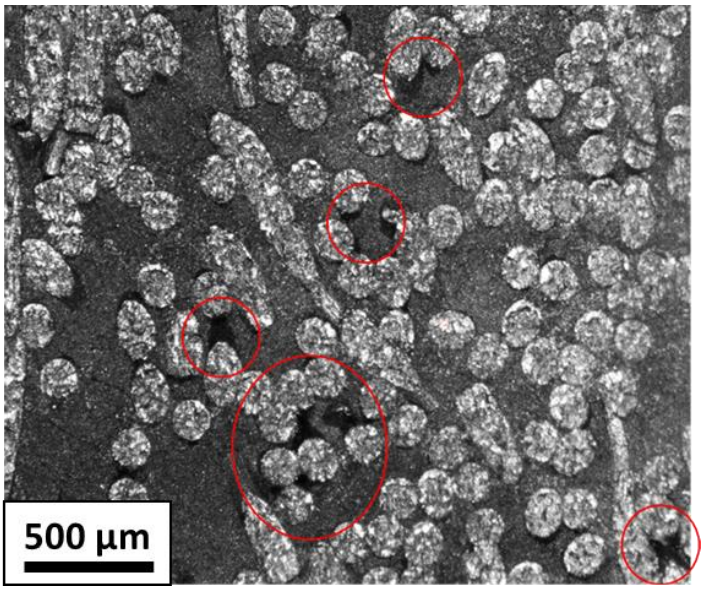

Figure 4 light microscope image showing microstructure overview for W_f/W1400 with 60% fiber mass fraction. Large voids formation can be observed. The contrast of the fibers is because of the over exposure effect of the fibers under light microscope.

Figure 5 represents the fiber grain structure of W_f/W1400 and W_f/W1550 compared to the as-fabricated fiber. The grain size across the axis of the wire is also measured showing in the Figure The cross section of the fiber is prepared by focus ion beam (FIB) without chemical etching. Compared to the as-fabricated state, much larger grain structure can be observed. This is due to the recrystallization of the fibers during FAST process. On the other hand, both W_f/W1400 and W_f/W1550 give similar fiber grain size. The grain sizes are measured based on the Lineal Intercept Procedure (ASTM E 112).

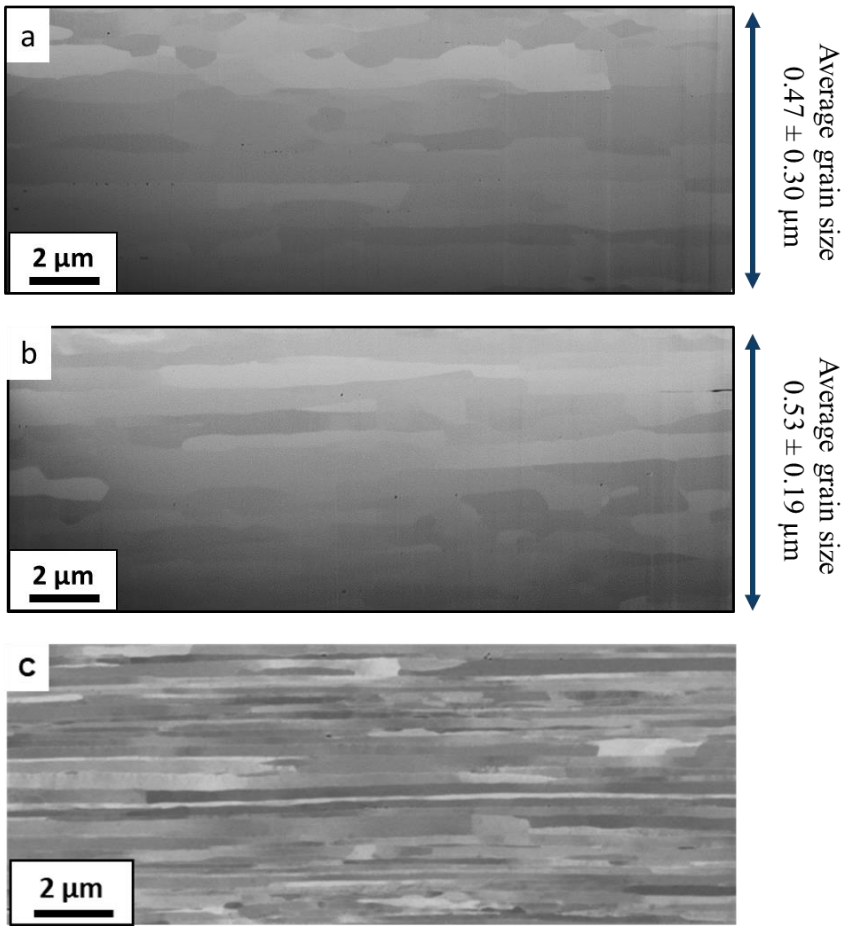

Figure 5 SEM image (SE, 3 kV accelerating voltage) showing fiber grain structure of W_f/W1400 (a), W_f/W1550 (b) and as-fabricated W fiber (c). The cross section of the fiber is prepared by focus ion beam (FIB) without chemical etching, the grain sizes of W_f/W1400 and W_f/W1550 are across the axis of the wire

To find out of the mechanical properties of the fibers after sintering, compared to the as-fabricated fibers, hardness tests (HV1) are performed. The results are shown in Figure 6. Due to the enlarged grain size and reduction of dislocation density during the high temperature FAST process, the fiber hardness in both W_f/W1400 and W_f/W1550 decreased compared to the as-fabricated state. However, the fiber hardness in W_f/W1400 and W_f/W1550 are in a similar range, which indicates a comparable mechanical properties of the fibers in the two cases.

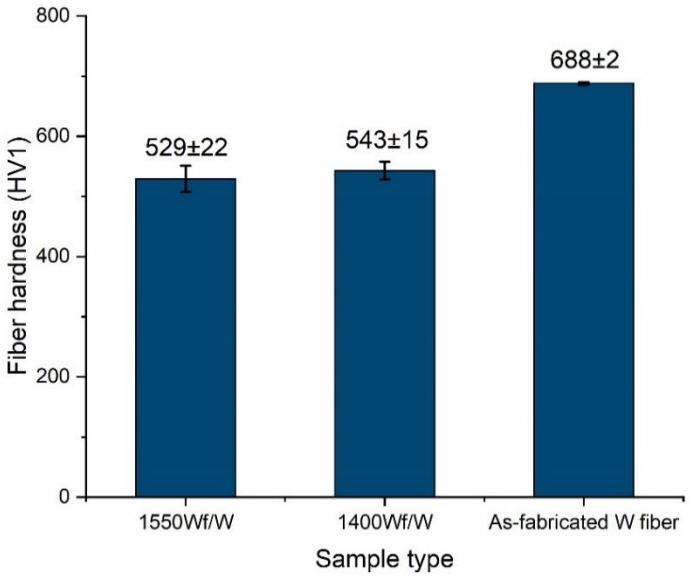

Figure 6 hardness tests (HV1) of the fibers for W_f/W1400, W_f/W1550 and as-fabricated state.

The force-displacement curves of the 3-point bending test are shown in Figure 7 and Figure 8. From force-displacement curves, it can be seen that, a pseudo ductile behavior [14] can be established by all the porous matrix W_f/W samples: after an linear-elastic deformation, the slope of the curve changes gradually to negative values after several small load drops; then a massive load-drop happens after reaching the maximum force; afterwards, the samples tend to have a stepwise or continuous load-decreasing. Even after large deformation (vertical bending displacement >0.3 mm), the sample remains as a whole with a strength of over 50 N.

For both W_f/W1400 and W_f/W1550, with the increasing of the fiber mass fraction, the maximum load increases. But the fiber mass fraction does not change the shape of the force-displacement curves. On the other hand, different fracture behavior can be observed for W_f/W1400 and W_f/W1550. Compared to W_f/W1550 with the same fiber mass fraction, W_f/W1400 samples tend to show a slightly lower maximum load but a more continuous load decreasing after reaching the maximum load (pseudo-plastic area). For W_f/W1550, sharper load drops can be observed.

In-situ monitoring is performed during the tests to observe the crack opening behavior. Typical cracking propagation paths for porous matrix W_f/W are shown in Figure 9. Due to the existence of the fibers, intensive crack deflection effect can be observed, similar to the behavior in [39].

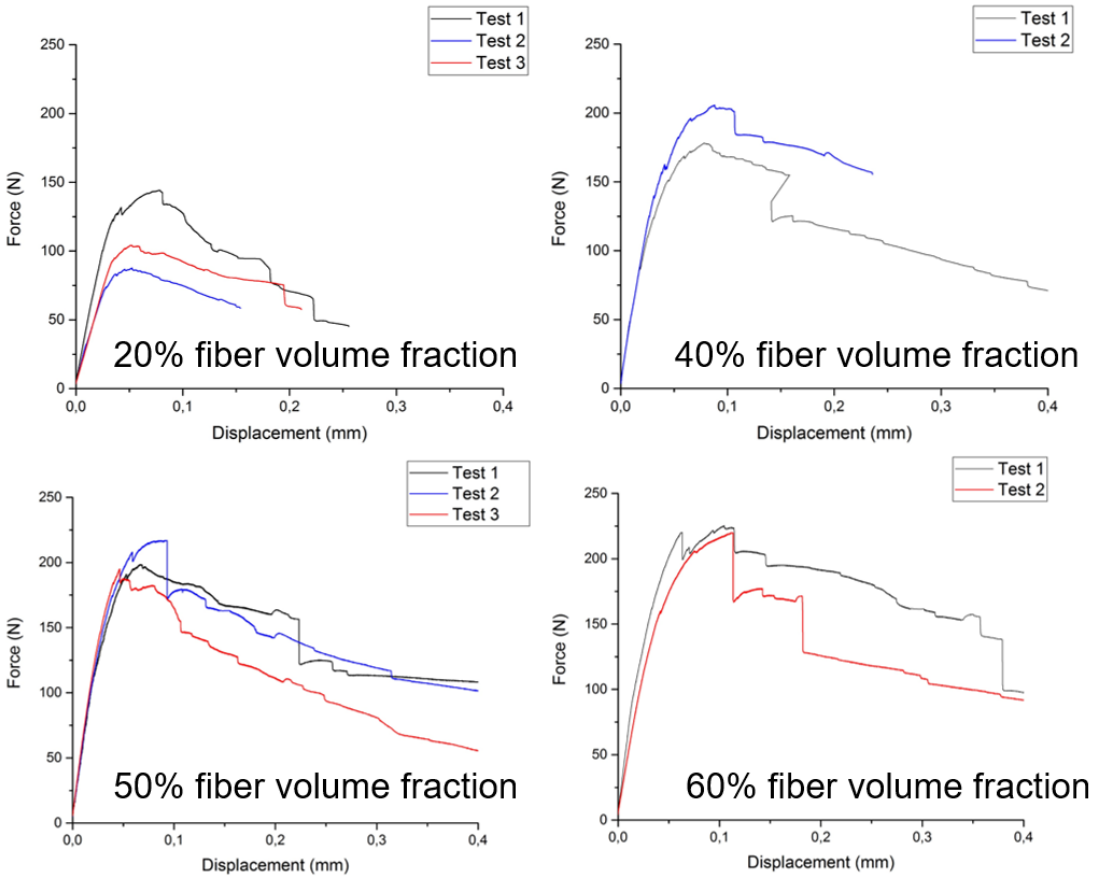

Figure 7 Fracture behavior of W_f/W1400 with different fiber mass fraction

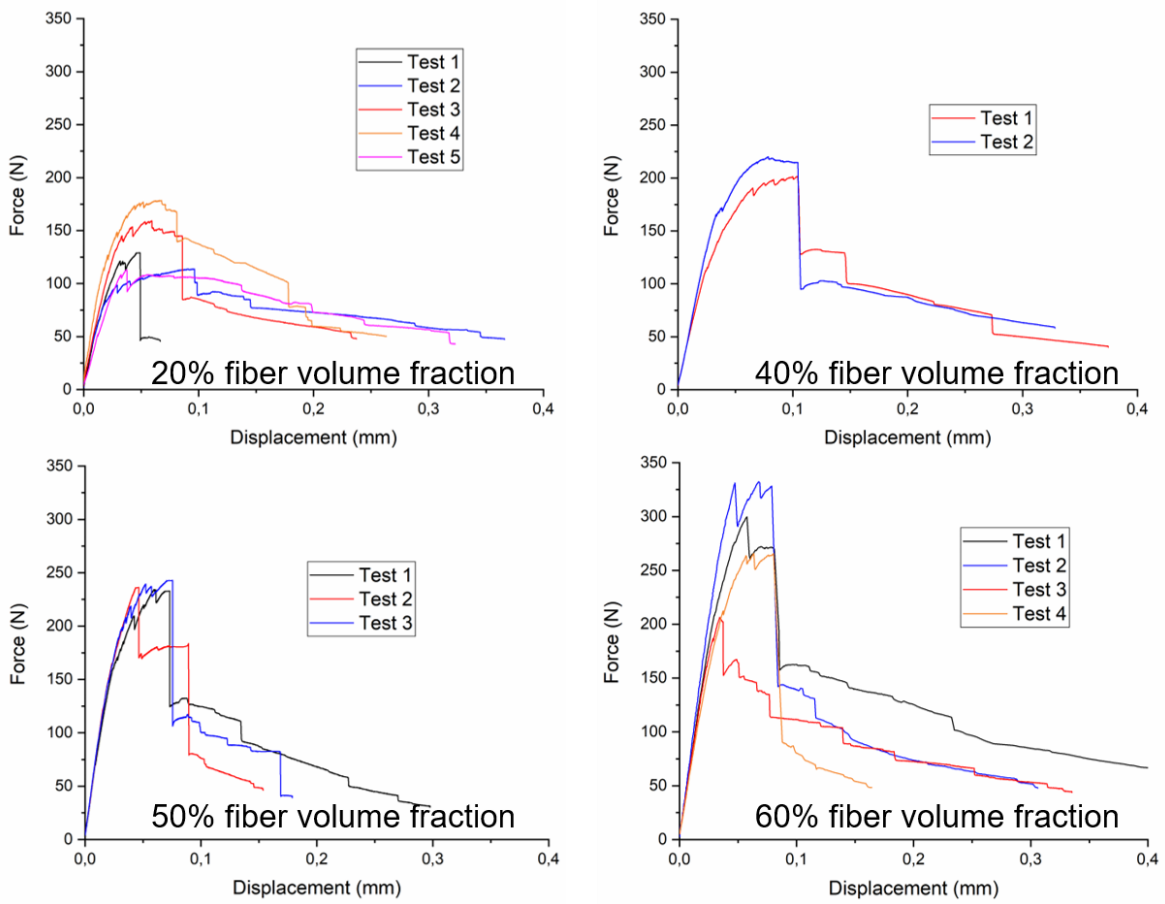

Figure 8 Fracture behavior of W_f/W1550 with different fiber mass fraction

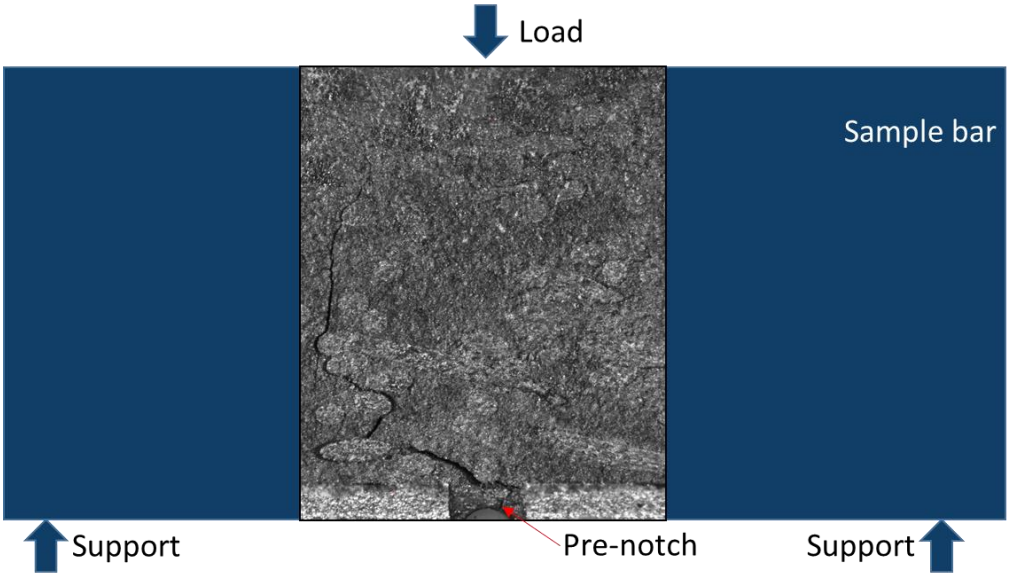

Figure 9 typical in-situ monitoring of crack propagation during 3-point bending test:

W_f/W1550 (1550 °C) with 40% fiber mass fraction

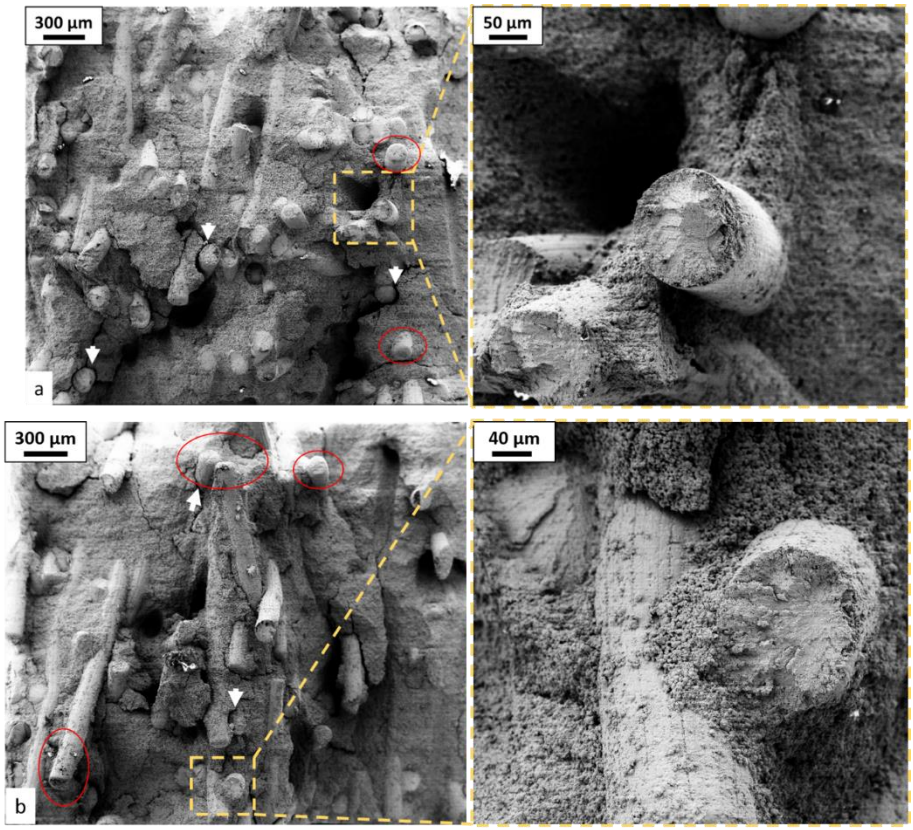

Figure 10 SEM image (SE, 10 kV accelerating voltage) showing fracture surface of W_f/W1400 (a) and W_f/W1550 (b) with 40% fiber mass fraction after 3-point bending test. The white arrows mark the de-bonding of the fibers and the red circles indicate the clear fiber ends

The SEM analysis on the fracture surfaces 3-point bending test are shown in Figure 10. For both samples, uneven topology of the surface is an indication for crack deflection. Additionally, fiber/matrix interface de-bonding is observed. Fiber pull-out effect is also observed. Some clear fiber ends without fracture are also visible, indicating the fiber-ends pull-out from the matrix without breakage.

Based on the measured force-displacement curves and the observed stable cracking length as mentioned in the experimental section, fracture energy density and fracture toughness can be calculated as shown in Table 3. Regarding fracture toughness, W_f/W1550 samples have higher

values compared to W_f/W1400 samples with the same fiber volume fraction. This is mainly because of the higher maximum load during the tests as shown in Figure 7 and Figure 8. It indicates that the materials can bear higher load under the condition of stable crack propagation. The maximum load is determined by the interface strength. When shear stress at the interface excesses the interface strength, massive fiber pull-out causes a load decreasing.

Table 3 fracture energy density and fracture toughness for porous matrix W_f/W with different fiber mass fraction

	20%	30%	40%	50%	60%
WfW1400 fracture toughness (MPa $m^{0.5}$)	-	12±5	17±2	22±10	26±7
WfW1550 fracture toughness (MPa $m^{0.5}$)	20±4	-	21±7	24±7	44±17
WfW1400 fracture energy density (kJ/mm^2)	-	1.9±0.6	6.1±0.1	7.8±4.3	9.2±2.0
WfW1550 fracture energy density (kJ/mm^2)	2.4±1.1	-	3.3±1.0	2.5±0.5	4.1±1.7

However, the fracture energy densities of the W_f/W1550 samples are lower than those of W_f/W1400 with the same fiber volume fraction. This is due to the different fiber/matrix bonding condition, which will be further discussed in Section 4. For W_f/W1550, a higher force is required to break the metallurgical bonding between fiber and matrix. This becomes an overloading after the interface debonding, leading to an unstable crack propagation. For W_f/W1400, the fiber and matrix are bonded mainly frictionally. Less overloading and unstable cracking are involved. A stable frictional fiber pull-out effect can occur. The stable frictional fiber pull-out consumes more energy compared to the brittle debonding effect of a metallurgical

bonding.

For both Wf/W1400 and Wf/W1550, the fracture toughness and fracture energy density increase with increasing fiber volume fraction. This can be attributed to the much higher mechanical properties of the tungsten fibers compared to tungsten matrix [28, 40]. Generally, with increasing fiber volume fraction, the difficulty of a crack need to pass through the material and the energy consumption required are higher, leading to higher fracture toughness and fracture energy density.

To measure the strength of the composites, 4-point bending tests are carried out. For each data point, 4 tests are performed. The average flexural strengths are shown in Figure 11. The error bars are the standard deviation of the tested values. It can be seen that, with increasing fiber mass fractions, both W_f/W1400 and W_f/W1550 have an increasing flexural strength until 50% mass fraction. A decrease of flexural strength can be measured when the fiber mass fraction is higher than 50%. Apart from samples with 60% fiber mass fraction.

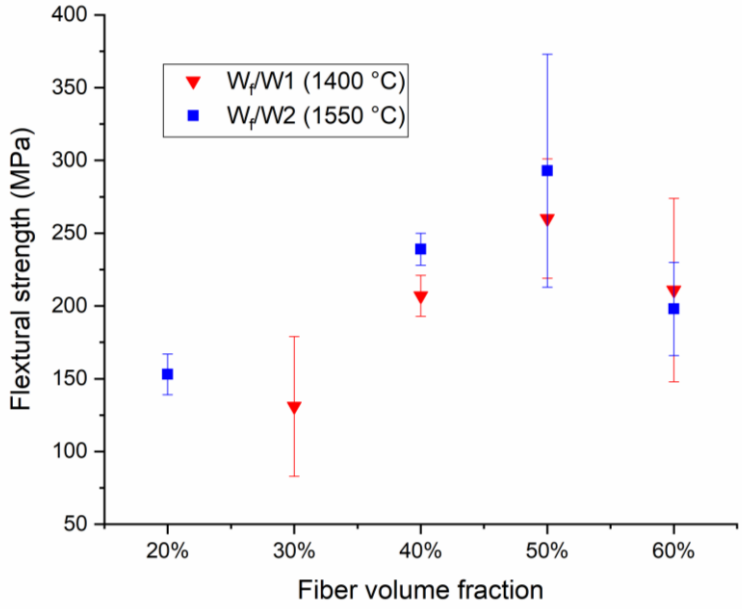

Figure 11 Flexural strength of porous matrix W_f/W with different fiber mass fraction, compared to conventional W_f/W

The thermal conductivity of porous matrix W_f/W1400_40% is shown in Figure 12, compared to reference pure W. It can be seen from the results, the thermal conductivity of porous matrix is ~66% of the value for pure W [41] due to the higher porosity.

The CTE of W_f/W1550 with 40% fiber mass fraction is measured by dilatometer. The measured average CTE between room temperature and 400 °C is (5.0±0.24) x10^{-6}/K. This value is close to the theoretical CTE of pure W, which is 4.5x10^{-6}/K based on literature [42].

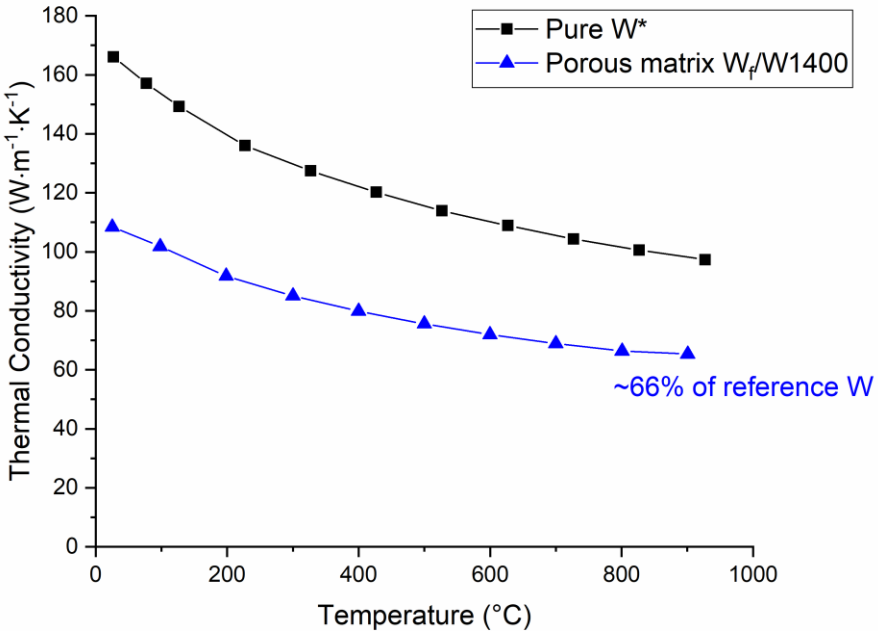

Figure 12 thermal conductivity of porous matrix W_f/W1400 with 40% fiber mass fraction (~81% density), compared to the reference pure W

4. Discussion

Bonding condition and fracture behavior

From Figure 7 and Figure 8, it can be seen that, all the types of porous matrix W_f/W tested show pseudo ductile behavior. However, there is still an obvious difference of the fracture behavior between W_f/W1400 and W_f/W1550. For W_f/W1400, the force decreases gradually after reaching the maximum load. While for W_f/W1550 a sudden load drop is observed. This

difference can be referred to the different fiber/matrix interface strength, leading to a different de-bonding behavior.

During the FAST process, W_f/W1400 are sintered at a lower temperature compared to W_f/W1550. Therefore, a relatively weaker bonding are formed. It can be seen from Figure 3, for W_f/W1400, the interface is very porous without dense connection. For W_f/W1550, the fiber and matrix are partially sintered together, leading to a metallurgical bonding between each other. To verify this assumption, a FIB prepared interface cross sections for both W_f/W1550 and W_f/W1400 are shown in Figure 13. It shows that some grains at the fiber/matrix interface form metallurgical bonding with the fiber for W_f/W1550. On the other hand, such metallurgical bonding is obvious for W_f/W1400. The difference in interface condition has a great influence on the fracture behavior [14]. A schematic diagram of the fiber de-bonding behavior during fiber pull-out process depending on interface condition is shown in Figure 14.

For W_f/W1400, the interface is in principle frictionally bonded with limited metallurgical bonding. In this case, the de-bonding process is always stable until a complete de-bonding, since the frictional force decreases linearly during the fiber pulling-out. This stress-displacement curve is typically no appreciable load drop after complete de-bonding (as shown in Figure 14 left). The maximum de-bonding stress is approximately equal to the incipient frictional pull-out stress [43]. This continuous load decreasing behavior results in a relative higher fracture energy consumption (area below the force-displacement curves), compared to W_f/W1550.

For the case of W_f/W1550, since the sintering temperature is higher, metallurgical bonding between fiber and matrix is formed to some extent. During the interface de-bonding, stable de-

bonding can proceed until the critical de-bonding length has been reached. At this point, the shear stress formed at the interface is equal to the metallurgical bonding strength. The strength difference between metallurgical bonding and frictional pull-out leads to an overload. This overload causes an unstable de-bonding leading to a sudden load drop. Therefore, the de-bonding process is partially stable (as shown in Figure 14 right).

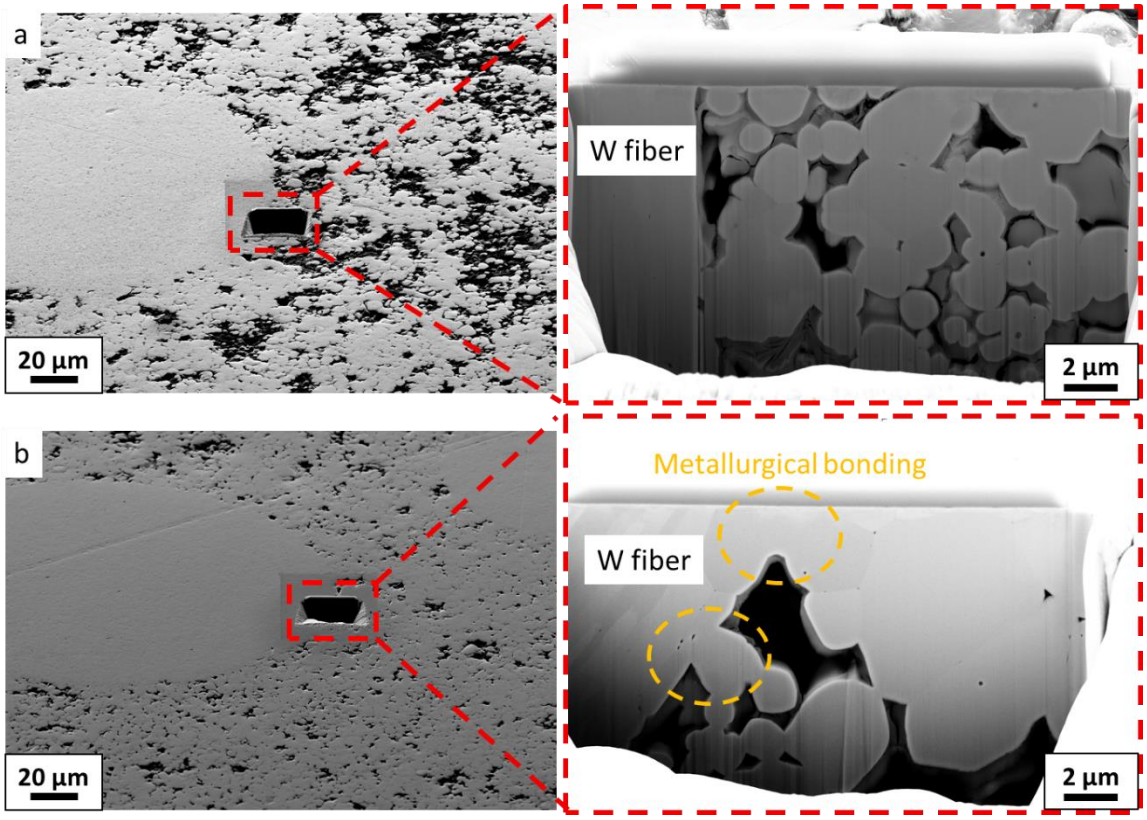

Figure 13 SEM image (SE, 3 kV accelerating voltage) showing FIB prepared interface cross sections for (a) W_f/W1400 and (b) W_f/W1550 with 40% showing the fiber/matrix bonding condition

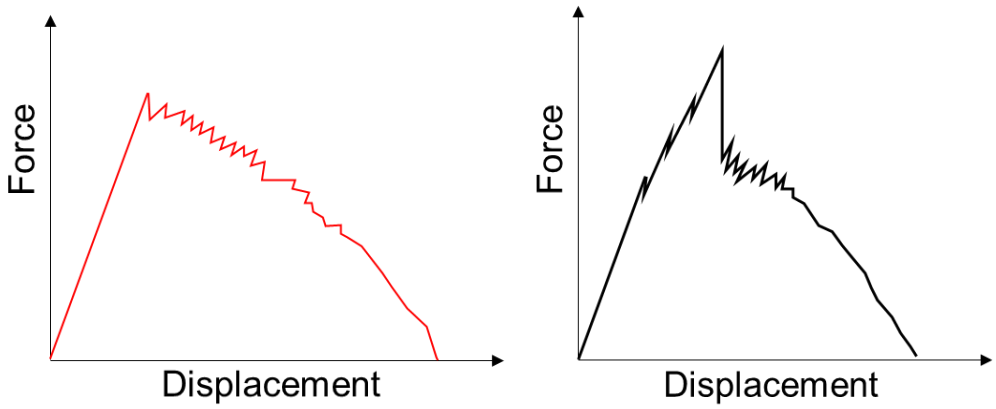

Figure 14 Schematic diagram of applied stress versus displacement relationship in fiber pull-out tests: (left) totally stable de-bonding process; (right) partially stable de-bonding process

Based on the abovementioned discussion, it can be seen that the sintering temperature has a great influence on the fracture behavior for porous matrix W_f/W. To clarify this point more clearly, two extra samples are produced using FAST with the same parameters as W_f/W1400 and W_f/W1550, only changing the sintering temperature to 1300 °C and 1900 °C. These two samples are aiming for a very weak and a very strong bonding between fiber and matrix, respectively. However, for the sample sintered at 1300 °C, due to the really low density of the matrix (~73%), losing edges occur during the 3-point bending tests. A valid force-displacement curve cannot be achieved. Only fracture surface is shown here. Figure 15 interprets the sintering temperature influence on the fracture behavior of porous matrix W_f/W.

For the sample sintered at 1300 °C, it can be seen from Figure 15, the tungsten powders are not effectively sintered. The tungsten matrix consists of loose round tungsten powders. The incomplete sintering process leads to a very low interface strength. During the bending test, with the increasing load, the shear stress at the interface can cause a direct interface de-bonding and fiber pull-out without a fiber fracture [44, 45]. In this case, the strength of the fibers is not

fully utilized. As it can be seen from Figure 15, for the sample that sintered at 1300 °C (~73% relative density), no fiber fracture is visible on the fracture surface. For the sample sintered at 1400 °C, as discussed before, mainly frictional bonding is formed between fiber and matrix. This bonding condition leads to a continuous load decrease after the maximum force. For the sample sintered at 1550 °C, partially metallurgical bonding is formed. The shear stress that needs to break the metallurgical bonding causes an overload for the composite, which lead to a sudden load drop after the maximum force. For the sample sintered at 1900 °C, the fiber and matrix are sintered together, forming very strong metallurgical interface (similar to the effect has been explained also in [14]). The composite, in this case, behave more like a bulk material. Extrinsic toughening mechanisms is no longer effective.

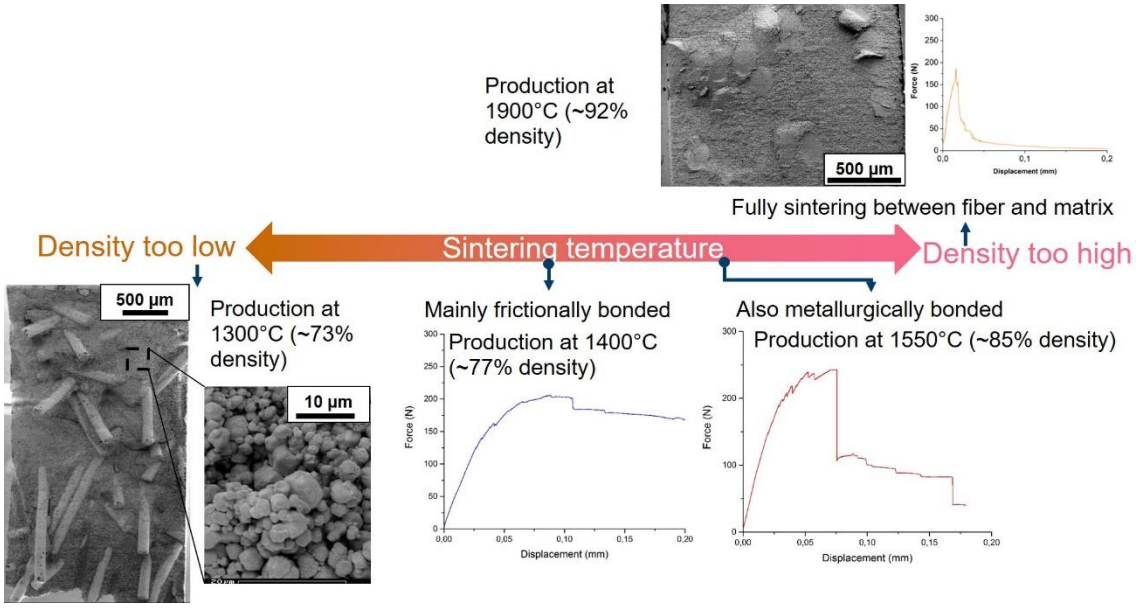

Figure 15 Sintering temperature influence on fracture behavior of porous matrix W_f/W

Material strength and fiber volume fraction

Generally, the strength of composite should increase with the increasing fiber volume fraction, as the fibers have much higher strength of the matrix. The strength of the composites can be

estimated by the rule of mixture [46, 47]:

$$\sigma_c = \sigma_f \cdot V_f + \sigma_m \cdot (1 - V_f) \tag{5}$$

Where σ_c, σ_f and σ_m are the average strength of the composites, fibers and matrix, respectively. V_f is the fiber mass fraction. From this equation, it can be seen that, higher matrix strength leads to higher composite strength.

The results in this work is consistent with the theory if the fiber volume fraction is lower than 50%, as it can be seen from Figure 11. However, when the fiber mass fraction is too high (to 60% in this case), there will be large voids formation due to a miss of powder to fill space between fibers, as it can be seen from Figure 4. The large voids can act as pre-damages before the matrix cracking. The inner damages acts, during loading, as crack initiation points, which will guide the crack propagation without cutting the fibers, as it can be seen from Figure 16. The crack behavior and material strength are, hence, deteriorated. This is the reason that for W_f/W, with a fiber mass fraction higher than 50%, a degradation of material strength can be observed.

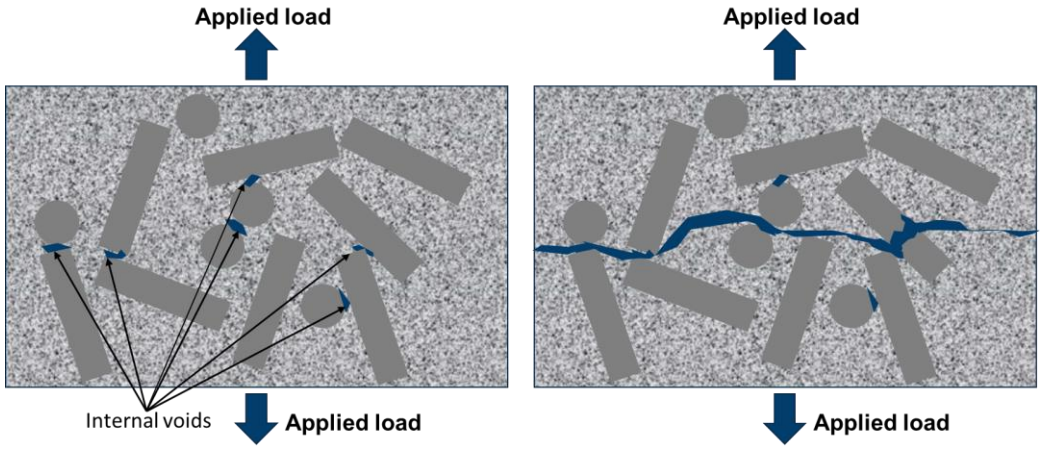

Figure 16 Schematic presentations of fracture propagation through porous matrix W_f/W, for samples with too high fiber mass fraction. The inhomogeneous powder-fiber mixing causes the formation of voids after sintering

Thermal properties

The thermal conductivity of porous matrix is ~66% of the value for pure W. This decreasing of the thermal conductivity property will indeed have some influence on the heat exhaust when using as high temperature facing materials. This may lead to a higher surface temperature and thermal stress. However, this decreased thermal conductivity may still be acceptable when considering the significantly increased mechanical properties. This need to be verified in the future with high heat load tests.

About the coefficient of thermal expansion, it is a very important material parameter when the W_f/W is joint with the cooling structure material. Based on our measurement, the increasing of porosity does not show a great influence on the CTE, which is also in line with the related theories [48]. It confirms that, the previous researches on joint process based on pure W can be applied also for porous matrix W_f/W. This would ease the application of W_f/W material, as a substitute/alternative of pure W, especially as the plasma facing component in future fusion reactor.

Summary and outlook

In this study, the influence of matrix density and fiber mass fraction on the mechanical behavior of porous matrix W_f/W are investigated. A series of samples with different fiber mass fraction and matrix density are produced and characterized. Based on the mechanical testing, porous matrix W_f/W shows a pseudo ductile behavior. Relatively lower matrix density (W_f/W1400) is helpful to avoid the sudden load-drop of during crack opening. However, the lower density causes a decreasing of material strength. This different fracture behavior is attributed to the different fiber/matrix interface condition. By increasing fiber mass fraction from 20% to 50%,

porous matrix W_f/W facilitates improved mechanical properties. By further increasing the fiber mass fraction from 50% to 60%, a deterioration of mechanical properties is observed. This deterioration is caused by the formation of large voids inside the material due to the inhomogeneous densification during FAST process. The thermal conductivity of W_f/W is strongly influenced by the material density; the high porosity causes a degradation of the thermal conductivity. On the other hand, no significant change in terms of thermal expansion coefficient is observed when decreasing the matrix density. Based on the aforementioned results, W_f/W1500 with 50% fiber mass fraction gives the best mechanical properties, which is recommended for further characterization.

In the next step, high heat load tests (e.g. thermal shock tests) will be performed to further understand the influence of the reduced thermal conductivity. In addition, plasma exposure tests on porous matrix W_f/W are planned to investigate the plasma wall interaction. Erosion behavior, fuel retention can be influenced by the porous matrix, which need to be further studied for the future application in future energy system.

Acknowledgement

This work has been carried out within the framework of the EUROfusion Consortium and has received funding from the Euratom research and training programme 2014–2018 and 2019–2020 under grant agreement no. 633053. The views and opinions expressed herein do not necessarily reflect those of the European Commission. This work is supported by the National Natural Science Foundation of China (Grant Nos. 52020105014, 52001104), the Fundamental Research Funds for the Central Universities (Grant No. JZ2020HGQB0230, JZ2019HGBZ0113, PA2019GDZC0096), the Natural Science Foundation of Anhui Province

(Grant Nos. 201904b11020034, 1908085ME115), the High Education Discipline Innovation Project “New materials and Technology for Clean Energy” (B18018), the International Postdoctoral Exchange Fellowship Program of Helmholtz-OCPC (No. 20191010).

Reference

[1] I. Smid, M. Akiba, G. Vieider, L. Plöchl, Development of tungsten armor and bonding to copper for plasma-interactive components, J. Nucl. Mater. 258-263(Part 1) (1998) 160-172.

[2] V. Philipps, Tungsten as material for plasma-facing components in fusion devices, J. Nucl. Mater. 415(1) (2011) S2-S9.

[3] J.W. Coenen, S. Antusch, M. Aumann, W. Biel, J. Du, J. Engels, S. Heuer, A. Houben, T. Hoeschen, B. Jasper, F. Koch, J. Linke, A. Litnovsky, Y. Mao, R. Neu, G. Pintsuk, J. Riesch, M. Rasinski, J. Reiser, M. Rieth, A. Terra, B. Unterberg, W. Th, T. Wegener, J.H. You, L. Ch, Materials for DEMO and reactor applications—boundary conditions and new concepts, Phys. Scr. 2016(T167) (2016) 014002.

[4] G. Pintsuk, I. Bobin-Vastra, S. Constans, P. Gavila, M. Rödig, B. Riccardi, Qualification and post-mortem characterization of tungsten mock-ups exposed to cyclic high heat flux loading, Fusion Eng. Des. 88(9-10) (2013) 1858-1861.

[5] R. Neu, J. Riesch, J.W. Coenen, J. Brinkmann, A. Calvo, S. Elgeti, C. García-Rosales, H. Greuner, T. Hoeschen, G. Holzner, F. Klein, F. Koch, C. Linsmeier, A. Litnovsky, T. Wegener, S. Wurster, J.H. You, Advanced tungsten materials for plasma-facing components of DEMO and fusion power plants, Fusion Eng. Des. 109-111 (2016) 1046-1052.

[6] L. Romaner, C. Ambrosch-Draxl, R. Pippan, Effect of Rhenium on the Dislocation Core Structure in Tungsten, Phys. Rev. Lett. 104(19) (2010).

[7] Z.M. Xie, R. Liu, S. Miao, X.D. Yang, T. Zhang, X.P. Wang, Q.F. Fang, C.S. Liu, G.N. Luo, Y.Y. Lian, X. Liu, Extraordinary high ductility/strength of the interface designed bulk W-ZrC alloy plate at relatively low temperature, Scientific reports 5 (2015) 16014.

[8] L. Luo, J. Shi, J. Lin, X. Zan, X. Zhu, Q. Xu, Y. Wu, Microstructure and performance of rare earth element-strengthened plasma-facing tungsten material, Scientific reports 6 (2016) 32701.

[9] Y. Zhang, A.V. Ganeev, J.T. Wang, J.Q. Liu, I.V. Alexandrov, Observations on the ductile-to-brittle transition in ultrafine-grained tungsten of commercial purity, Materials Science and Engineering: A 503(1-2) (2009) 37-40.

[10] R. Liu, X. Xia, M.Y. Xie, C. Chen, S. Wang, Z.H. Zhong, L.F. Cao, Y.C. Wu, Effect of interlayers on the tensile behaviors of tungsten multilayered composites, Journal of Alloys and Compounds 827 (2020).

[11] H. Bolt, V. Barabash, G. Federici, J. Linke, A. Loarte, J. Roth, K. Sato, Plasma facing and high heat flux materials - Needs for ITER and beyond, J. Nucl. Mater. 307-311(1 SUPPL.) (2002) 43-52.

[12] R.A. Pitts, S. Carpentier, F. Escourbiac, T. Hirai, V. Komarov, S. Lisgo, A.S. Kukushkin, A. Loarte, M. Merola, A. Sashala Naik, R. Mitteau, M. Sugihara, B. Bazylev, P.C. Stangeby, A full tungsten divertor for ITER: Physics issues and design status, J. Nucl. Mater. 438 (2013) S48-S56.

[13] J. Linke, High heat flux performance of plasma facing materials and components under service conditions in future fusion reactors, Fusion science and technology 53(2T) (2008) 278-287.

[14] Y. Mao, J.W. Coenen, J. Riesch, S. Sistla, J. Almanstotter, B. Jasper, A. Terra, T. Hoschen, H. Gietl, C. Linsmeier, C. Broeckmann, Influence of the interface strength on the mechanical properties of discontinuous tungsten fiber-reinforced tungsten composites produced by field assisted sintering technology, Compos Part a-Appl S 107 (2018) 342-353.

[15] H. Gietl, A. von Muller, J.W. Coenen, M. Decius, D. Ewert, T. Hoschen, P. Huber, M. Milwich, J. Riesch, R. Neu, Textile preforms for tungsten fibre-reinforced composites, J. Compos. Mater. 52(28) (2018) 3875-3884.

[16] J.W. Coenen, Y. Mao, J. Almanstotter, A. Calvo, S. Sistla, H. Gietl, B. Jasper, J. Riesch, M. Rieth, G. Pintsuk, F. Klein, A. Litnovsky, A.V. Mueller, T. Wegener, J.H. You, C. Broeckmann, C. Garcia-Rosales, R. Neu, C. Linsmeier, Advanced materials for a damage resilient divertor concept for DEMO: Powder-metallurgical tungsten-fibre reinforced tungsten, Fusion Eng. Des. 124 (2017) 964-968.

[17] J. Riesch, J.Y. Buffiere, T. Höschen, M. di Michiel, M. Scheel, C. Linsmeier, J.H. You, In situ synchrotron tomography estimation of toughening effect by semi-ductile fibre reinforcement in a tungsten-fibre-reinforced tungsten composite system, Acta Mater. 61(19) (2013) 7060-7071.

[18] O.A. Waseem, H.J. Ryu, Toughening of a low-activation tungsten alloy using tungsten short fibers and particles reinforcement for fusion plasma-facing applications, Nucl. Fusion 59(2) (2019) 026007.

[19] D.M. Hulbert, A. Anders, D.V. Dudina, J. Andersson, D. Jiang, C. Unuvar, U. Anselmi-Tamburini, E.J. Lavernia, A.K. Mukherjee, The absence of plasma in “spark plasma sintering”, J. Appl. Phys. 104(3) (2008) 033305.

[20] O. Guillon, J. Gonzalez-Julian, B. Dargatz, T. Kessel, G. Schierning, J. Räthel, M. Herrmann, Field-Assisted Sintering Technology/Spark Plasma Sintering: Mechanisms, Materials, and Technology Developments, Advanced Engineering Materials 16(7) (2014) 830-849.

[21] G. Czél, M.R. Wisnom, Demonstration of pseudo-ductility in high performance glass/epoxy composites by hybridisation with thin-ply carbon prepreg, Compos Part a-Appl S 52 (2013) 23-30.

[22] H. Ming-Yuan, J.W. Hutchinson, Crack deflection at an interface between dissimilar elastic materials, Int. J. Solids Struct. 25(9) (1989) 1053-1067.

[23] F.W. Zok, C.G. Levi, Mechanical Properties of Porous-Matrix Ceramic Composites, Advanced Engineering Materials 3(1-2) (2001) 15-23.

[24] T.J. Mackin, J.Y. Yang, C.G. Levi, A.G. Evans, Environmentally compatible double coating concepts for sapphire fiber-reinforced γ-TiAl, Materials Science and Engineering: A 161(2) (1993) 285-293.

[25] J.J. Brennan, Interfacial characterization of a slurry-cast melt-infiltrated SiC/SiC ceramic-matrix composite, Acta Mater. 48(18) (2000) 4619-4628.

[26] Y. Mao, J.W. Coenen, S. Sistla, X. Tan, J. Riesch, L. Raumann, D. Schwalenberg, T. Höschen, C. Chen, Y. Wu, C. Broeckmann, C. Linsmeier, Development of tungsten fiber-reinforced tungsten with a porous matrix, Phys. Scr. T171 (2020).

[27] J. Riesch, J. Almanstötter, J.W. Coenen, M. Fuhr, H. Gietl, Y. Han, T. Höschen, C. Linsmeier, N. Travitzky, P. Zhao, R. Neu, Properties of drawn W wire used as high performance fibre in tungsten fibre-reinforced tungsten composite, IOP Conference Series: Materials

Science and Engineering 139 (2016) 012043.

[28] P. Zhao, J. Riesch, T. Hoschen, J. Almanstotter, M. Balden, J.W. Coenen, R. Himml, W. Pantleon, U. von Toussaint, R. Neu, Microstructure, mechanical behaviour and fracture of pure tungsten wire after different heat treatments, Int. J. Refract. Met. Hard Mater. 68 (2017) 29-40.

[29] J. Riesch, Y. Han, J. Almanstotter, J.W. Coenen, T. Hoschen, B. Jasper, P. Zhao, C. Linsmeier, R. Neu, Development of tungsten fibre-reinforced tungsten composites towards their use in DEMO-potassium doped tungsten wire, Phys. Scr. T167(T167) (2016) 014006.

[30] Y. Mao, C. Chen, J.W. Coenen, J. Riesch, S. Sistla, J. Almanstötter, A. Terra, Y. Wu, L. Raumann, T. Höschen, H. Gietl, R. Neu, C. Linsmeier, C. Broeckmann, On the nature of carbon embrittlement of tungsten fibers during powder metallurgical processes, Fusion Eng. Des. 145 (2019) 18-22.

[31] J.W. Coenen, Y. Mao, S. Sistla, J. Riesch, T. Hoeschen, C. Broeckmann, R. Neu, C. Linsmeier, Improved pseudo-ductile behavior of powder metallurgical tungsten short fiber-reinforced tungsten (Wf / W), Nuclear Materials and Energy 15 (2018) 214-219.

[32] K. Hu, X.Q. Li, C. Yang, Y.Y. Li, Densification and microstructure evolution during SPS consolidation process in W-Ni-Fe system, Transactions of Nonferrous Metals Society of China (English Edition) 21(3) (2011) 493-501.

[33] R. Ohser-Wiedemann, U. Martin, A. Müller, Fast sintering of mechanical alloyed Mo-W powders, Proceedings of the International Euro Powder Metallurgy Congress and Exhibition, Euro PM 2012, 2012.

[34] M. Rieth, A. Hoffmann, Influence of microstructure and notch fabrication on impact bending properties of tungsten materials, Int. J. Refract. Met. Hard Mater. 28(6) (2010) 679-

686.

[35] Prüfung metallischer Werkstoffe; Kerbschlagbiegeversuch; Besondere Probenform und Auswertungsverfahren. s.l., DIN 50115, Beuth-Verlag, 1991.

[36] A. E399-17, Standard Test Method for Linear-Elastic Plane-Strain Fracture Toughness KIc of Metallic Materials, ASTM International, West Conshohocken, PA, 2017.

[37] W. Schnell, D. Gross, W. Hauger, Technische Mechanik: Band 2: Elastostatik, Springer-Verlag2013.

[38] Y. Mao, J.W. Coenen, J. Riesch, S. Sistla, J. Almanstötter, A. Terra, C. Chen, Y. Wu, L. Raumann, T. Höschen, H. Gietl, R. Neu, C. Broeckmann, C. Linsmeier, Fiber Volume Fraction Influence on Randomly Distributed Short Fiber Tungsten Fiber-Reinforced Tungsten Composites, Advanced Engineering Materials 22(6) (2020).

[39] Y. Mao, J.W. Coenen, J. Riesch, S. Sistla, J. Almanstötter, J. Reiser, A. Terra, C. Chen, Y. Wu, L. Raumann, T. Höschen, H. Gietl, R. Neu, C. Linsmeier, C. Broeckmann, Fracture behavior of random distributed short tungsten fiber-reinforced tungsten composites, Nucl. Fusion 59(8) (2019) 086034.

[40] B. Gludovatz, S. Wurster, A. Hoffmann, R. Pippan, Fracture toughness of polycrystalline tungsten alloys, Int. J. Refract. Met. Hard Mater. 28(6) (2010) 674-678.

[41] J. Habainy, Y. Dai, Y. Lee, S. Iyengar, Thermal diffusivity of tungsten irradiated with protons up to 5.8 dpa, J. Nucl. Mater. 509 (2018) 152-157.

[42] P. Hidnert, W.T. Sweeney, Thermal expansion of tungsten, US Government Printing Office1925.

[43] J.-K. Kim, C. Baillie, Y.-W. Mai, Interfacial debonding and fibre pull-out stresses, J. Mater.

Sci. 27(12) (1992) 3143-3154.

[44] L. Greszczuk, Theoretical studies of the mechanics of the fiber-matrix interface in composites, Interfaces in composites, ASTM International1969.

[45] A. Bentur, S. Mindess, Fibre reinforced cementitious composites, CRC Press2006.

[46] V. Laws, The efficiency of fibrous reinforcement of brittle matrices, J. Phys. D: Appl. Phys. 4(11) (1971) 1737-1746.

[47] A. Kelly, G. Davies, The principles of the fibre reinforcement of metals, Metall. Rev. 10(1) (1965) 1-77.

[48] Q. Zeng, K. Li, T. Fen-Chong, P. Dangla, Effect of porosity on thermal expansion coefficient of cement pastes and mortars, Construction and Building Materials 28(1) (2012) 468-475.